Research Article Vol. 31, No. 5 / 27 Feb 2023 / Optics Express 7321
Optics EXPRESS

Near-field manipulation of Tamm plasmon polaritons

NANNAN LI,[1] QI ZOU,[1] BO ZHAO,[1] CHANGJUN MIN,[1] XIAOCONG YUAN,[1] MICHAEL SOMEKH,[1,2,3] AND FU FENG[1,*]

[1]Institute of Microscale Optoelectronics, Nanophotonics Research Center, Shenzhen Key Laboratory of Micro-Scale Optical Information Technology, Shenzhen University, Shenzhen 518060, China
[2]Faculty of Engineering, University of Nottingham, Nottingham NG7 2RD, UK
[3]mike.somekh@szu.edu.cn
[*]fufeng@szu.edu.cn

Abstract: Tamm plasmon polaritons (TPPs) arise from electromagnetic resonant phenomena which appear at the interface between a metallic film and a distributed Bragg reflector. They differ from surface plasmon polaritons (SPPs), since TPPs possess both cavity mode properties and surface plasmon characteristics. In this paper, the propagation properties of TPPs are carefully investigated. With the aid of nanoantenna couplers, polarization-controlled TPP waves can propagate directionally. By combining nanoantenna couplers with Fresnel zone plates, asymmetric double focusing of TPP wave is observed. Moreover, radial unidirectional coupling of the TPP wave can be achieved when the nanoantenna couplers are arranged along a circular or a spiral shape, which shows superior focusing ability compared to a single circular or spiral groove since the electric field intensity at the focal point is 4 times larger. In comparison with SPPs, TPPs possess higher excitation efficiency and lower propagation loss. The numerical investigation shows that TPP waves have great potential in integrated photonics and on-chip devices.

1. Introduction

Surface plasmon polaritons (SPPs) are electromagnetic waves propagating at the interface between a dielectric and a conductor, being confined evanescently in the direction which is perpendicular to the propagating surface. Owing to their high optical state confinement and large electromagnetic field enhancement, optical field manipulation using SPPs has been intensively investigated. Optical devices based on SPPs have been applied in a wide range of fields, including plasmon waveguides [1,2], surface enhanced Raman scattering [3,4], surface enhanced fluorescence [5,6], enhancement of nonlinear process [7,8], high-sensitivity sensing [9,10], super-resolution imaging [11,12], on-chip data processing [13,14], and plasmonic tweezers [15,16]. However, conventional SPPs have a few drawbacks. For instance, its excitation efficiency is not sufficiently high in certain applications. Moreover, SPPs suffer from severe propagation loss, which limits their applications in sensing and waveguides.

Tamm plasmon polaritons (TPPs), on the other hand, are a type of electromagnetic resonances which appear at the interface between a metallic film and a distributed Bragg reflector (DBR) [17–22]. Compared to SPPs, TPPs possess many intriguing characteristics. In TPPs, confinement of the optical field is achieved through total internal reflection and interferences in quasiperiodic structures of DBR [17]. TPPs can be excited by both transverse magnetic (TM) and transverse electric (TE) polarized light [18,19]. In addition, TPPs possess both cavity mode property derived from the Bragg gratings and surface plasmon characteristics [21]. TPPs present relatively low losses, resulting in sharper coupling resonance peaks and longer propagation distances in comparison with conventional SPPs [22]. These features endow TPPs with extra advantages, and their applications in different fields have been investigated. For example, confined TPPs under

#481440 https://doi.org/10.1364/OE.481440
Journal © 2023 Received 22 Nov 2022; revised 19 Jan 2023; accepted 22 Jan 2023; published 14 Feb 2023

Optics EXPRESS

metallic microdisks have been applied to control spontaneous emission of single quantum dots [17]. TPPs have been applied to enhanced nonlinear optical effects, such as second-harmonic and third-harmonic generation enhancement [22–24]. In addition, confined TPP mode and hybrid TPP/SPP mode have been applied as surface-emitting lasers [21,25], perfect light absorbers [26–29], narrowband thermal emitters [30–32], refractive index sensors [33–35], and narrow bandpass filters [36]. To our knowledge, however, all of the former studies merely focus on the confined cavity mode property of TPPs, while surface propagation characteristics of TPPs has hardly been explored.

In this paper, we numerically investigate the generation and propagation properties of TPPs. TPPs are successfully excited on a structure which consists of a silver film, DBR multilayers and a dielectric substrate. The propagation properties of TPPs are carefully studied by introducing nanoantennas in the structure. With the aid of nanoantenna couplers, TPP waves can propagate directionally under incident light with different polarizations. By combining nanoantenna couplers with Fresnel zone plates, asymmetric double focusing of TPP wave is observed. Radial unidirectional coupling of TPPs can be achieved when the nanoantenna couplers are arranged along a circular or in an Archimedes spiral shape, which show superior focusing ability compared to a single circular or spiral groove since the electric field intensity at the focal point is 4 times larger. Our results show that TPPs possess higher excitation efficiency and lower propagation loss than SPPs. TPPs can be a promising supplement to SPPs in near-field manipulation of light. The numerical investigation of TPPs shows that TPPs can be potentially applied in polarization state analysis, chiral structure detection, integrated photonics, and on-chip device design.

2. Principle and modeling

The proposed structure for generating TPPs is schematically sketched in Fig. 1(a). This system consists of three parts: a silver film (top), DBR multilayers (middle) and a dielectric substrate (bottom). The DBR multilayers are composed of ten pairs of alternating TiO_2/SiO_2 layers with a TiO_2 spacer on the top. The refractive indexes of TiO_2 and SiO_2 were set as $n_h = 2.37$ and $n_l = 1.45$, respectively. The refractive index of the dielectric substrate should be high enough to excite high-order modes [27,37,38], so it was set as $n_s = 2.00$. The thicknesses of alternating TiO_2 and SiO_2 layer in each unit were set as $d_h = 56.2$ nm and $d_l = 91.9$ nm, which satisfies the Bragg conditions ($n_h \cdot d_h = n_1 \cdot d_1 = \lambda/4$) [39]. The thicknesses of the silver film and TiO_2 spacer were set as $d_{Ag} = 50$ nm and $d_{spacer} = 70$ nm. Although we only perform numerical simulations in this study, we would like to propose the possible process to fabricate this structure. The dielectric multilayers can be fabricated via plasma-enhanced chemical vapor deposition of SiO_2 and TiO_2 on a dielectric substrate [40]. The 50-nm-thick Ag film can be deposited onto the multilayers via electron-beam evaporation with a 5-nm Ge adhesion layer [41]. The structures of nanoslits can be fabricated using focused ion beam milling [41]. The dielectric function of silver was calculated through the Drude model

$$\varepsilon_m(\omega) = \varepsilon_\infty - \frac{\omega_p^2}{\omega^2 + i\gamma\omega} \tag{1}$$

where high-frequency constant $\varepsilon_\infty = 3.4$, plasma frequency $\omega_p = 1.39 \times 10^{16}$ rad/s, and scattering rate $\gamma = 2.7 \times 10^{13}$ rad/s [42,43]. The structure was illuminated by a plane wave from the bottom. Finite element methods (FEM) were employed to numerically calculate the absorption and reflection spectra as well as electric field distribution of this structure. Perfectly matched layer (PML) boundary conditions were utilized on all sides in simulations. A global mesh of λ/10 is applied to the entire structure, and an additional mesh of λ/20 is applied to the region of nanoslits. The monitor was placed at the Ag/DBR interface. In our study, the working wavelength λ was chosen as 633 nm. The *xz*-plane electric field distribution of this structure under normal

Optics EXPRESS

incidence is shown in Fig. 1(b). The real part of refractive index of the structure is also plotted for comparison. The electric field reaches maximum at the position which is 45 nm below the Ag/DBR interface, and decays gradually and periodically within the DBR multilayers. The confinement of energy at the Ag/DBR interface reveals the successful excitation of TPP mode. TPP mode can be understood using the Fabry-Perot cavity resonance model [18]. In this model, TPP mode is treated as travelling light which is resonantly trapped between two imaginary cavity mirrors, as schematically illustrated in Fig. 1(c). By using the transfer matrix method, the resonance condition can be obtained by solving the eigenmode equation for the field at metal/DBR interface as

$$r_{\mathrm{m}} \cdot r_{\mathrm{DBR}} \cdot \exp(2i\delta) = 1 \tag{2}$$

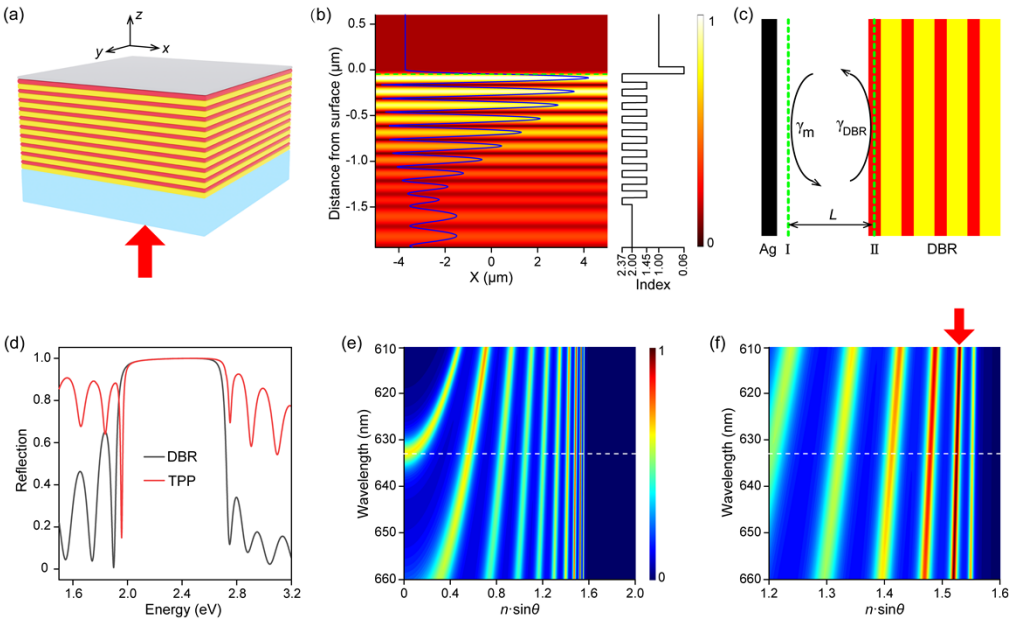

Fig. 1. The structure for generating TPPs. (a) Schematic of the structure which is composed of a Ag film (top), DBR multilayers (middle) and a glass substrate (bottom). The red arrow represents the incident beam; (b) The *xz*-plane electric field distribution of the structure (left) and real part of refractive index of the structure (right) under normal incidence. The blue curve refers to the electric field. The green dashed line indicates the position of the Ag/DBR interface; (c) Schematic illustration of the Fabry-Perot cavity resonance model for TPP mode; (d) Reflection spectra of the DBR multilayers and TPP structure under normal incidence; (e) Dispersion relation of the structure described by absorption as a function of $n{\cdot}\sin\theta$ under the incident light with TE polarization. The white dashed line indicates the wavelength of 633 nm. (f) Dispersion relation of the structure described by absorption under TE polarized incidence with a finer scale. (e) and (f) share the same color scale bar. The red arrow indicates the position of the dominant high-order mode.

Therefore, the phase of the TPPs should satisfy

$$\mathrm{Arg}[r_{\mathrm{m}} \cdot r_{\mathrm{DBR}} \cdot \exp(2i\delta)] = 2m\pi \tag{3}$$

where r_{m} and r_{DBR} are the amplitude reflection coefficients for the propagating wave at metal side and at DBR side, respectively. δ refers to phase shift of the wave propagating across the cavity, and m represents the order of the TPP mode ($m = 0, 1, 2\ldots$). In our study, the DBR structure

Optics EXPRESS

is designed with an energy bandgap over the range of [1.899, 2.749] eV and the bandgap is centered at the energy $E_{\mathrm{DBR}} = 2.324$ eV (533.5 nm), as shown in Fig. 1(d). When a metallic layer is deposited on the DBR multilayers, the TPP mode appears as a dip in the reflection spectrum with an energy given by [17]

$$E_{\mathrm{Tamm}} = \frac{E_{\mathrm{DBR}}}{1 + \eta E_{\mathrm{DBR}}/E_{\mathrm{plasma}}} \tag{4}$$

$$\eta = 2\frac{|n_{\mathrm{h}} - n_{\mathrm{l}}|}{\pi\sqrt{\varepsilon_{\mathrm{B}}}} \tag{5}$$

where n_{h} and n_{l} are the refractive indices of the DBR multilayers, ε_{B} is the background dielectric constant, and E_{plasma} is the plasma energy of the metal. With the presence of a silver film, the TPP mode energy is calculated to be $E_{\mathrm{Tamm}} = 1.957$ eV (633.4 nm), which is consistent with the simulated result (Fig. 1(d)). Figure 1(e) shows the dispersion relation of this structure described by absorption as a function of $n{\cdot}\sin\theta$ under the incident light with TE polarizations, where n and θ refers to the refractive index of the substrate and the incidence angle, respectively. Figure 1(f) also shows the dispersion relation of this TPP structure under TE polarized incidence but with a finer scale to present the results more clearly. According to the dispersion relations, there are multiple modes excited on this TPP structure, while the dominant one is the high-order mode which lies in the position where $n{\cdot}\sin\theta = 1.525$ (as indicated by the red arrow in Fig. 1(f)). This is the reason for choosing high-refractive-index substrate, otherwise the high-order mode cannot be excited. In addition, the slope of the high-order mode in Fig. 1(f) is proportional to the group velocity of the propagation mode. More details of this high-order mode will be discussed in the following part.

3. Results and discussion

In order to perform near-field manipulation of TPPs, nanoantennas are introduced in the TPP structure. Introducing nanoantennas have two advantages, it can facilitate the excitation of high-order mode owing to scattering and can control the direction of the propagation wave. Nanoantennas are not necessary to excite the high-order mode, because the high-order mode of the TPP structure can be excited under the incidence of plane wave at a specific angle. But nanoantennas do facilitate the excitation of high-order mode owing to scattering, since the incidence angle will not be limited. In this study, the nanoantennas are designed as rectangular nanoslits within the silver film. The length, width and height of the nanoslits were set as 200 nm, 40 nm and 50 nm, respectively. The TPP structure was illuminated by a plane wave from the bottom at normal incidence. The *xz*-plane electric field distribution of the structure with a nanoslit is shown in Fig. 2(a). The electric field reaches maximum near the Ag/DBR interface, which is similar to the electric field distribution shown in Fig. 1(b) except that there is propagating wave at the Ag/DBR interface. To confirm whether the propagation wave corresponds to the dominant high-order mode, we calculate the effective wavelength of the high-order mode as follows

$$\lambda_{\mathrm{eff}} = \frac{\lambda_0}{n\sin\theta} \tag{6}$$

where λ_0 is the wavelength of the incident light (633 nm). λ_{eff} is calculated as 415 nm when $n{\cdot}\sin\theta = 1.525$ (as indicated by the red arrow in Fig. 1(f)). The wavelength of 415 nm is consistent with the wavelength calculated from the phase profile as shown in Fig. 2(b) and Fig. 2 (c), which indicates that it is the high-order TPP mode ($\lambda_{\mathrm{TPP}} = 415$ nm). Figure 2(b) and Fig. 2(c) show the H_z components at the *xy* plane launched by a single nanoslit with orientation of 45° (b) and 135° (c), respectively, under left circularly polarized (LCP) incident light. The target *xy* plane is the Ag/DBR interface. It shows that a high-aspect-ratio nanoslit can be treated as a dipole

Optics EXPRESS

source oscillating along its long axis, which selectively scatters incident light with polarizations perpendicular to its orientation [44]. The electric fields launched by these two nanoslits possess a phase difference of π/2 determined by their orientation angles [45,46]. In contrast, the phase difference of the electric fields launched by these two nanoslits changes to –π/2 under right circularly polarized (RCP) incident light.

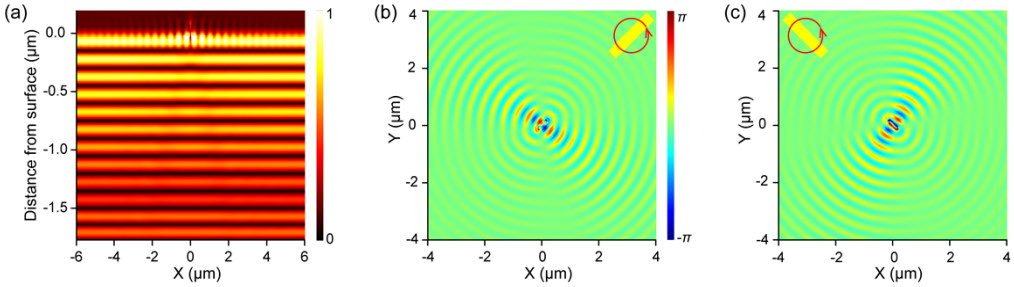

Fig. 2. TPP structure with a single nanoslit. (a) The *xz*-plane electric field distribution of the structure with a nanoslit under normal incidence. (b,c) The H_z components at the *xy* plane launched by a nanoslit with orientation of 45° (b) and 135° (c) under LCP excitation. (b) and (c) share the same color scale bar.

Each single nanoslit can be treated as a dipole source. By superposing electric field generated from each dipole source, the overall electric field can be obtained. The overall electric field generated by the nanoantenna array can be expressed as

$$\vec{E}(\vec{r}) = i\omega\mu_0 \sum_{m=1}^{N} \vec{G}(\vec{r}, \vec{r}_m)\vec{p}(\vec{r} - \vec{r}_m)e^{i\varphi_m} \tag{7}$$

where ω is the angular frequency of the incident light, μ_0 is the free-space permeability, N is the number of nanoslits. $\vec{G}(\vec{r}, \vec{r}_m)$ is the Green dyadic tensor. $\vec{p}(\vec{r} - \vec{r}_m)$ represents a dipole located at position $\vec{r}_m$. The phase term φ_m denotes the relative phase difference between dipole sources. Equation (7) shows that the amplitude and phase of the electric field launched by the nanoantenna array can be tuned by changing the tilt angle of the nanoslits. Specifically, we consider the field distribution generated by a pair of nanoantennas consisting of two nanoslits with orientations of 135° and 45°, as shown in Fig. 3(a). By using the quasi-plane wave approximation, the electric field at the dashed line launched by the nanoantenna pair under LCP excitation can be expressed as

$$\vec{E}_{\text{plane}} = \vec{E}_1 e^{i\Delta\varphi_1} + \vec{E}_2 e^{i\Delta\varphi_2} = \vec{E}_1 e^{ik(s+L)} + \vec{E}_2 e^{ikL} \tag{8}$$

where k is the wavevector of the TPP wave, $\vec{E}_{\text{plane}}$ is the electric field at the target plane, $\vec{E}_1$ and $\vec{E}_2$ are the electric field generated by the line-1 nanoantenna array and line-2 nanoantenna array, respectively. s is the distance between line 1 and line 2, and L is the distance between line 2 and target dashed line. As mentioned above, the electric field launched by nanoslits oriented at 135° and 45° has a phase delay of –π/2, which means

$$\vec{E}_1 = \vec{E}_2 e^{-i\frac{\pi}{2}} = E_0 e^{i\alpha} e^{-i\frac{\pi}{2}} \tag{9}$$

where E_0 and α are the initial amplitude and phase of electric field. Equation (8) can therefore be simplified as

$$\begin{aligned}\vec{E}_{\text{plane}} &= \vec{E}_2 e^{ik(s+L)-i\frac{\pi}{2}} + \vec{E}_2 e^{ikL} = E_0 e^{i\alpha} e^{ikL}\left\{e^{i\left(ks-\frac{\pi}{2}\right)} + 1\right\} \\ &= E_0 e^{i\alpha} e^{ikL}\left\{e^{i\frac{\pi}{2}\left(\frac{4s}{\lambda_{\text{TPP}}}-1\right)} + 1\right\}\end{aligned} \tag{10}$$

Optics EXPRESS

where λ_{TPP} is the effective wavelength of the TPP wave. According to Eq. (10), the constructive interference can be observed when $s = (n + 1/4)\lambda_{TPP}$ ($n = 0, 1, 2\ldots$), and the destructive interference can be observed when $s = (n + 3/4)\lambda_{TPP}$. Schematic of the TPP structure with chiral nanoantenna array is shown in Fig. 3(b). In this nanoantenna array, s was set as 5/4 λ_{TPP}, and the y-axis distance d between two nanoslits was designed as 300 nm. The distance between two adjacent double-line was set as 2 λ_{TPP}, and the nanoantenna array consisted of 9 double-line nanoantenna pairs. The electric field intensity ($|E|^2$) launched by the nanoantenna array under LCP and RCP incident light are shown in Fig. 3(c) and 3(d), respectively. It can be clearly observed that most of the energy is scattered to the right (left) side under LCP (RCP) excitation, which is consistent with the former theoretical analysis. The results show that the designed nanoantenna array is sensitive to the polarization states of the incident light, and the propagation direction of the TPP wave can be precisely controlled.

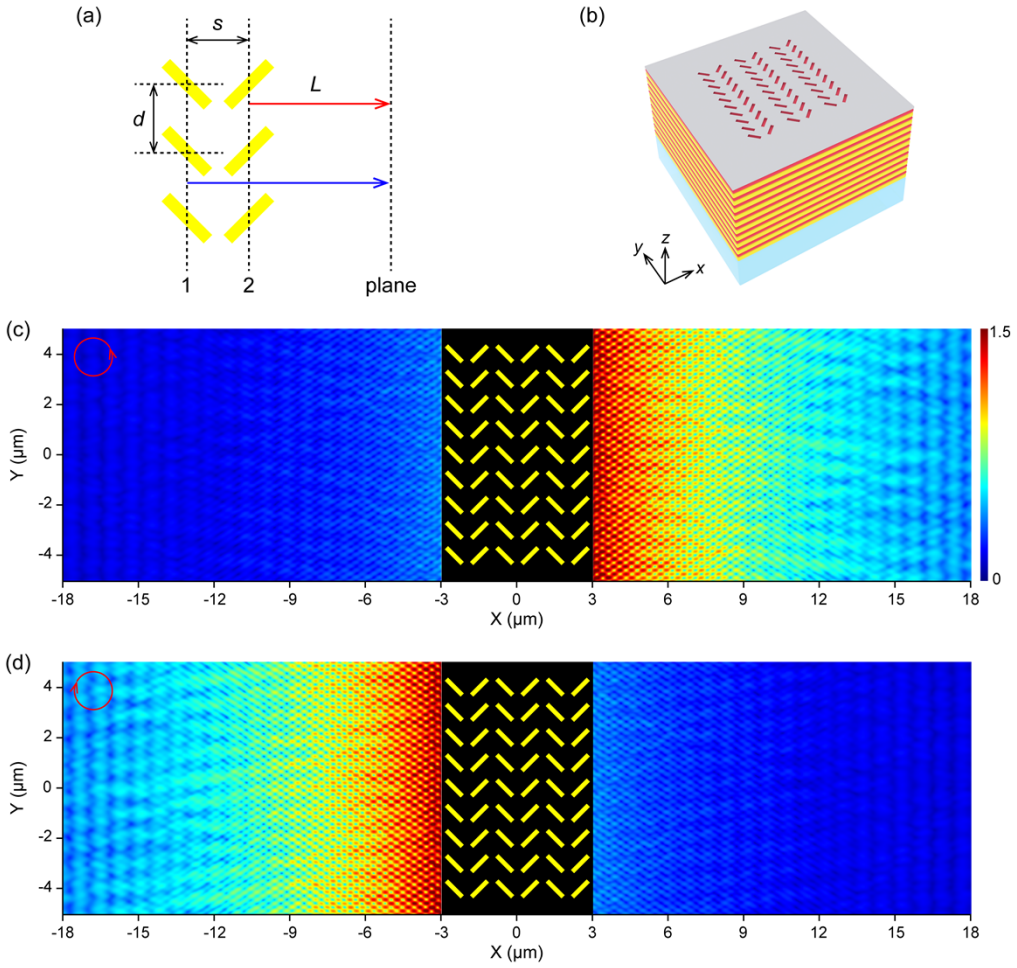

Fig. 3. TPP structure with chiral nanoantenna array. (a) Schematic of the double-line nanoantenna array; (b) Schematic of the TPP structure with chiral nanoantenna array; (c,d) Electric field intensity ($|E|^2$) distribution launched by the nanoantenna array under LCP (c) and RCP (d) incident light. (c) and (d) share the same color scale bar.

As a comparison, the propagation behavior of SPPs is also investigated. The structure for generating SPPs is schematically sketched in Fig. 4(a). This structure consisted of an Ag film

Optics EXPRESS

(top) and a glass substrate (bottom). This structure was illuminated by a plane wave from the bottom at normal incidence. The target *xy* plane is the top surface of this SPP structure. The thickness of the Ag film was set as 50 nm, which is the same with the TPP structure. The nanoslits with the same dimensions are also introduced within the Ag film. In the nanoantenna array, the distance between two lines with different orientations was set as 5/4 λ_{SPP}, and the distance between two adjacent double-line was set as 2 λ_{SPP}. λ_{SPP} is the effective wavelength of the SPPs, which can be calculated as [44]

$$\lambda_{SPP} = \mathrm{Re}\left\{2\pi/\left(\frac{\omega}{c_0}\sqrt{\frac{\varepsilon_d\varepsilon_m}{\varepsilon_d+\varepsilon_m}}\right)\right\} \tag{11}$$

where ε_d and ε_m are the dielectric constant of the air and the Ag film, respectively. Please note the target interface is the Ag/air interface instead of the Ag/glass interface. λ_{SPP} is calculated to be 610 nm. The electric field intensity launched by the nanoantenna array under LCP and RCP incident light are plotted in Fig. 4(b) and 4(c), respectively. Similarly, most of the energy is scattered to the right (left) side under LCP (RCP) excitation. Furthermore, dispersion and loss of propagation wave (including SPPs and TPPs) can be characterized using the propagation length. The propagation length L_p is defined as the energy decay length for wave propagating along the surface or the interface. The electric field intensity at position x along the propagation direction can be expressed as [47]

$$I = I_0 e^{-x/L_p} \tag{12}$$

where I_0 is the initial electric field intensity. The propagation length L_p of SPPs and TPPs is calculated by fitting the electric field intensity profiles, as plotted in Fig. 4(d) and Fig. 4(e). The electric field intensity profiles are calculated by averaging the intensity along the y axis. The fitting equation for TPPs is I_{TPP} = 1.386*exp(-x/12.235), and the fitting equation for SPPs is I_{SPP} = 0.684*exp(-x/8.405). The fitting coefficient R^2 for these two fittings are both over 0.97. The initial electric field intensity of TPPs (1.386) is twice as large as that of the SPPs, which indicates that the excitation efficiency of TPPs is much higher than that of SPPs. The high excitation efficiency of TPPs is derived from the interference of light reflected by different dielectric interfaces. In addition, the two fitting equations were normalized for comparison, as shown in Fig. 4(e). It clearly shows that the propagation length of TPPs (12.235 μm) is approximately 1.5 times larger than that of SPPs (8.405 μm). The large propagation length arising from the low loss property of TPPs is favorable for applications such as sensing and waveguides. Considering that the effective wavelength of TPPs (415 nm) is smaller than that of SPPs (610 nm), the effective propagation length (the ratio of propagation length to effective wavelength, L_p/λ_{eff}) of TPPs (29.48) is 2.14 times larger than that of SPPs (13.78). The twofold increase in the effective propagation length means that more complex processing can be used without the need for additional amplification. Taken together, TPPs exhibit superior propagation properties compared to SPPs in higher excitation efficiency and lower propagation loss. Therefore, TPPs can be a promising supplement for SPPs in near-field manipulation of light.

Combining the Fresnel zone plate (FZP) and the nanoantenna array together, polarization controlled focusing of TPP wave can be achieved. By arranging the y-axis position of the nanoslits according to the radius profile of the FZP, the focal length of the TPP wave can be precisely controlled. The radius profile of the FZP can be expressed as [48]

$$R_m = \sqrt{mf\lambda_{TPP} + \frac{m^2}{4}\lambda_{TPP}^2} \tag{13}$$

where m describes each radius of the FZP (m = 1,2,3. . .), and f refers to the focal length. R_m should be larger than the distance between the neighboring nanoantennas, so the curvature of the circular FZP zone can be ignored. The FZP is integrated with the nanoantenna array by removing

Optics EXPRESS

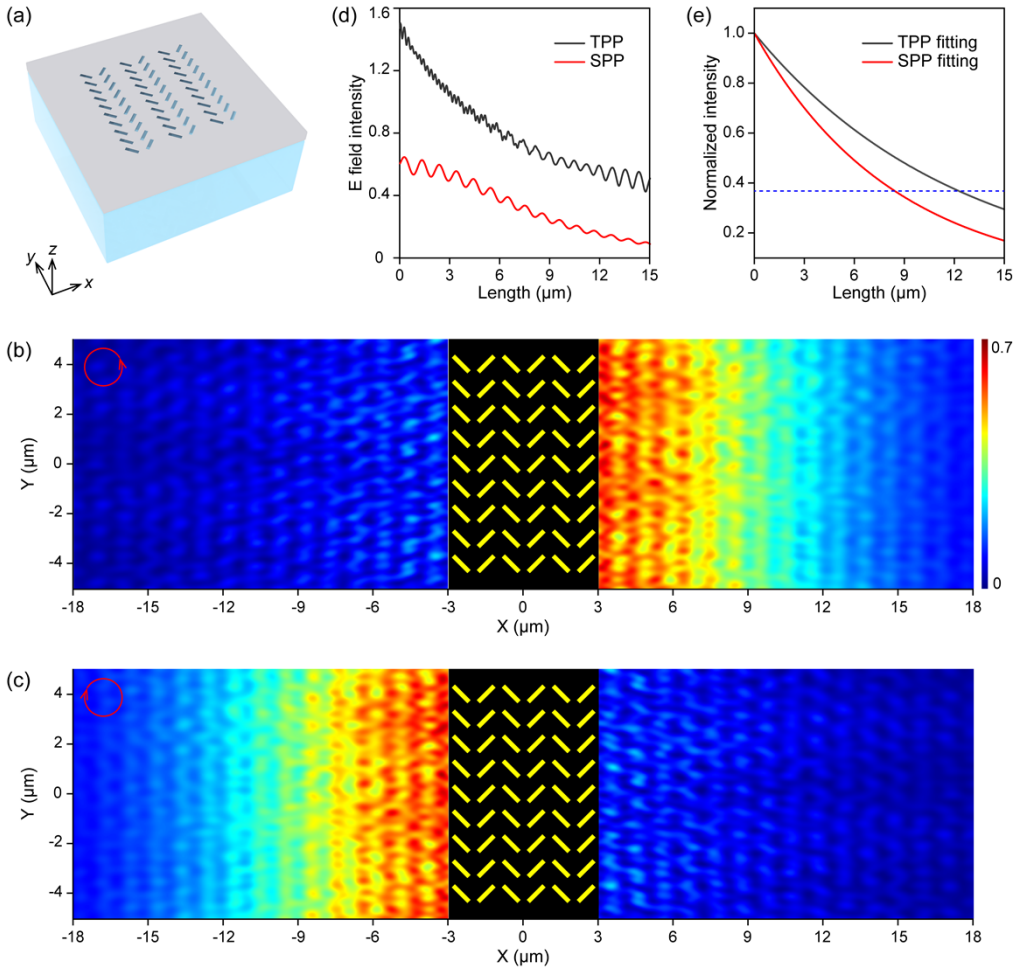

Fig. 4. SPP structure with chiral nanoantenna array. (a) Schematic of SPP structure which is composed of an Ag film (top) and a glass substrate (bottom). This structure was illuminated by a plane wave from the bottom; (b,c) Electric field intensity distribution launched by the nanoantenna array under LCP (b) and RCP (c) excitation. (b) and (c) share the same color scale bar. (d) Electric field intensity as a function of the propagation length for TPPs and SPPs. (e) Normalized fitting equations as a function of the propagation length for TPPs and SPPs. The blue dashed line indicates the intensity of 1/*e*.

the nanoslits falling within the region of R_2–R_1, R_4–R_3, R_6–R_5, etc [48]. Figure 5(a) shows the electric field intensity launched by the FZP nanoantenna array under LCP excitation. Most of the energy is scattered towards the right side, and TPP wave is efficiently focused with a focal length of 15 μm. For the same structure, TPP wave is focused at the left side with the same focal length under RCP excitation due to the symmetry. The focal length can be precisely controlled by adjusting the parameters of the FZP nanoantenna array according to Eq. (13).

Although the FZP nanoantenna array mentioned above could achieve directional focusing of the TPP wave, however, the right-side and left-side focal lengths are always the same. To obtain double focusing of the TPP wave with different focal lengths, a hybrid FZP nanoantenna array is employed. The key idea is to discover three different types of nanoantenna pairs which can launch TPP wave to left side, right side and bidirectional side. As discussed above, TPP wave

Optics EXPRESS

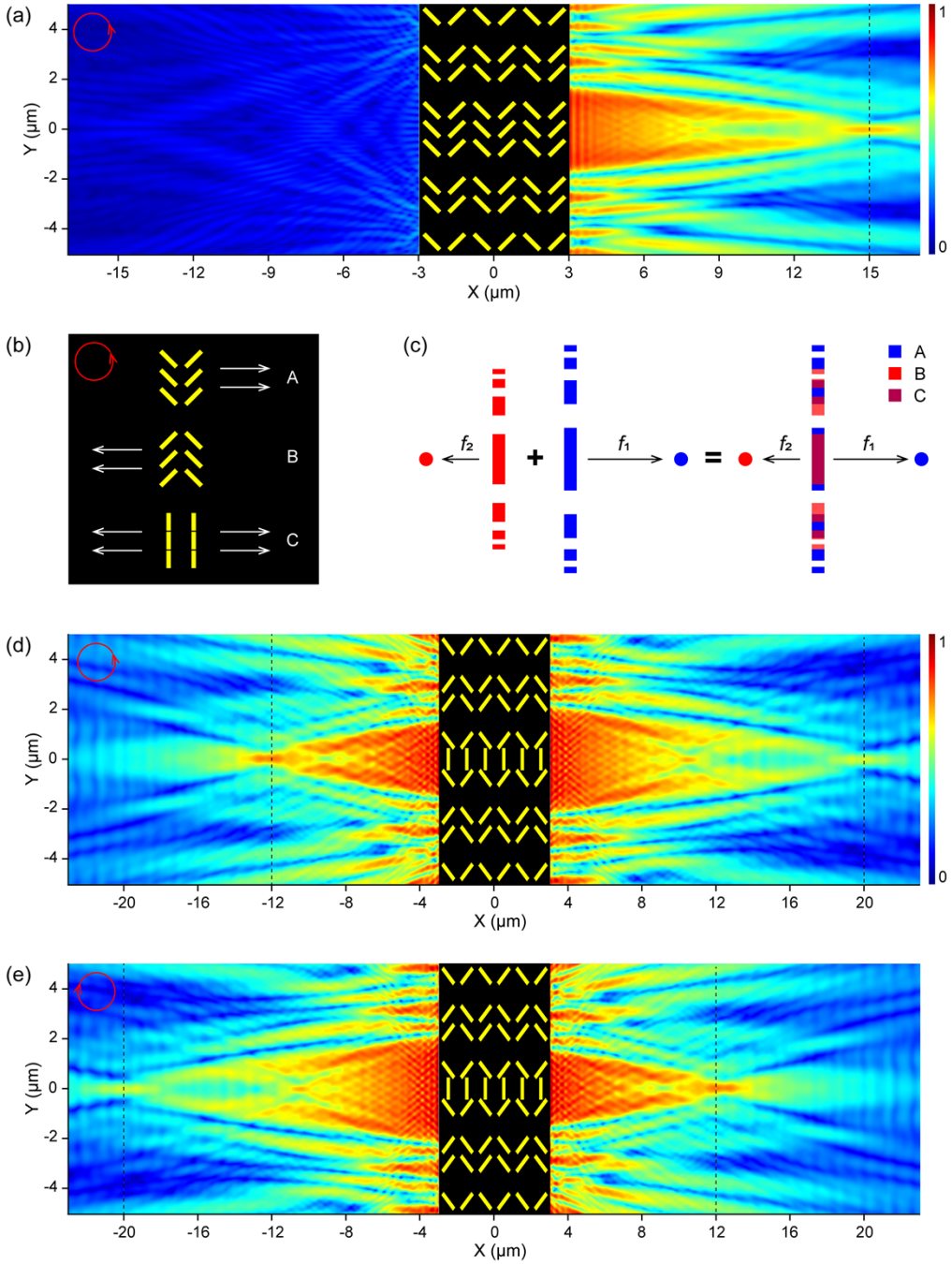

Fig. 5. FZP nanoantenna array. (a) Electric field intensity distribution launched by the designed FZP nanoantenna array under LCP excitation. The black dashed line indicates the position of the focal length. The color scale bar is normalized; (b) Schematic of the three different types of nanoantenna pairs; (c) Schematic of the design principle of the hybrid FZP nanoantenna array; (d,e) Electric field intensity distribution launched by the hybrid FZP nanoantenna array under LCP (d) and RCP (e) excitation. The black dashed lines indicate the positions of the focal length. (d) and (e) share the same normalized color scale bar.

Optics EXPRESS

launched by a pair of nanoslits with orientations of 135° and 45° can propagate to the right side under LCP excitation. Symmetrically, TPP wave launched by two nanoslits with orientations of 45° and 135° can propagate to the left side. As Fig. 5(b) shows, under LCP excitation, the type-A, type-B and type-C nanoantenna pairs can launch TPP wave to the right side, left side and both sides, respectively. The design principle of the hybrid FZP nanoantenna array is illustrated in Fig. 5(c). For the focal length towards right side f_1 and the focal length towards left side f_2, the corresponding y-axis positions of these nanoantenna pairs ($R_m(|f_1|)$ and $R_m(|f_2|)$) are calculated according to Eq. (13). The absolute value of the focal lengths ($|f_1|$ and $|f_2|$) is determined by the y-axis position of the nanoantenna pairs, while the direction of the focal point (left side or right side) is determined by the types of nanoantenna pairs. As Fig. 5(c) shows, type-A nanoantenna pairs with focal length f_1 are placed in blue region, type-B nanoantenna pairs with focal length f_2 are placed in red region, and type-C nanoantenna pairs are placed in overlap region. Figure 5(d) shows the electric field intensity launched by the hybrid FZP nanoantenna array under LCP excitation. The focal lengths at right side and left side are 20 μm (f_1) and 12 μm (f_2), respectively. It presents an asymmetric focusing behavior. On the other hand, under RCP excitation, the TPP waves launched by the type-A and type-B nanoantenna pairs switch to left side and right side, respectively. As a result, the focal lengths at right side and left side of the same structure can be switched by simply changing the polarization of the incident light from LCP to RCP, as shown in Fig. 5(e). The results prove that asymmetric double focusing of the TPP wave can be achieved by designing the parameters of the hybrid FZP nanoantenna array. The proposed manipulation method can be potentially applied in plasmonic switches, tunable lenses and optical sensing.

Radial unidirectional coupling of TPP wave can be achieved by arranging the nanoantenna pairs along a circular shape. As Fig. 6 shows, the nanoantenna pairs were placed with an angular interval of 5° and the radius of the circle was set as 4 μm. Under LCP excitation, TPP wave launched by the circular nanoantenna array can propagate outward (Fig. 6(a)), and the field intensity approaches zero within the circle. Under RCP excitation, TPP wave can propagate radially toward the center of the circle (Fig. 6(b)). The distances from each nanoantenna pairs to the center are all the same, so the phase differences of the electric filed at the center is identical. As a result, there is a bright focal point at the center together with several standing waves within the circle. As comparison, the electric field intensity launched by a single circular groove under LCP (Fig. 6(c)) and RCP (Fig. 6(d)) excitation are the same since the circular groove is achiral. In these cases, the energy of the electric field propagating inward and outward is equal, so the electric field intensity ($|E|^2$) at the focal point is only 1/4 to the electric field intensity launched by circular nanoantenna pairs. In other words, circular nanoantenna pairs exhibit superior focusing ability compared to a single circular groove since the electric field intensity at the focal point is 4 times larger. By replacing the single circular groove into a circular nanoantenna array, the handedness of the incident light can be clearly distinguished and the electric field intensity at the focal point can be remarkably enhanced.

The near-field manipulation of TPP wave can be further generalized by adding more chiral element into the nanoantenna array. Archimedes spiral is a typical type of chiral structures which has been used as polarization analyzer [49–52]. As Fig. 7(a) shows, the nanoantenna pairs are arranged along a left-handed Archimedes spiral shape, and the symmetry axes of the nanoantenna pairs (the red dashed line) are perpendicular to the radial direction of the spiral. The position of each nanoantenna pair is defined as (in polar coordinate)

$$r = r_0 + n\lambda_{TPP} \cdot \frac{\theta}{2\pi} \tag{14}$$

where r is the distance from the central point O to the nanoantenna pair, r_0 is the starting distance, θ is the azimuthal angle, and n is a positive integer number ($n = 1,2,3\ldots$). In this study, the nanoantenna pairs were placed with an angular interval of 6°, r_0 was set as 2.2 μm, and n was chosen as 3. The electric field distribution near the center of the spiral nanoantenna array is

Optics EXPRESS

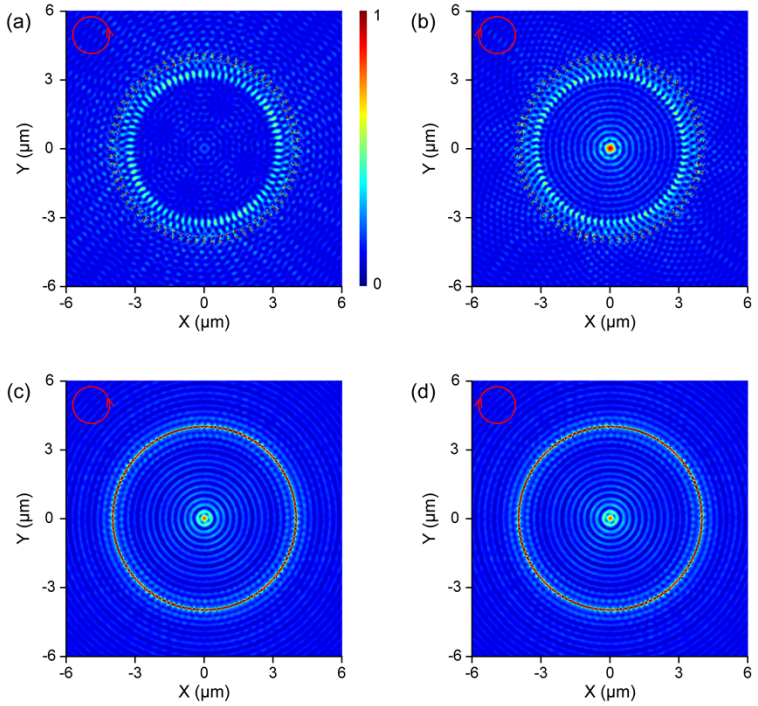

Fig. 6. Circular nanoantenna array. (a,b) Electric field intensity distribution launched by the circular nanoantenna array under LCP (a) and RCP (b) excitation; (c,d) Electric field intensity distribution launched by the single circular groove under LCP (c) and RCP (d) excitation. (a–d) share the same normalized color scale bar.

theoretically analyzed. As Fig. 7(b) shows, for the nanoantenna pair with the coordinate (r, θ), the electric field of the incident light in xy plane can be decomposed as

$$\vec{E}_0 = E_0 \cos(\varphi - \theta)\vec{u} + E_0 \sin(\varphi - \theta)\vec{v} \tag{15}$$

where φ is the polarization angle, u is the component of E_0 that is perpendicular to the symmetry axis (blue dashed line) of the nanoantenna pairs, and v is the component of E_0 that is parallel to the symmetry axis. Since only the component perpendicular to the symmetry axis can excite TPP wave that reach the center, we focus on the u component. Thus, the electric field near the center can be approximately written as (in cylindrical coordinate (ρ, α, z)) [52]

$$\vec{E}_1(\rho, \alpha, z) = E_0 \cos(\phi - \theta) e^{-\kappa z} e^{i[\varphi + \vec{k}_{\mathrm{TPP}} \cdot (\vec{\rho} - \vec{r})]} \vec{n} \tag{16}$$

where $\vec{n}$ is a unit vector, $\Phi(\theta)$ describes the additional phase introduced by the incident light, and $\Phi(\theta) = \pm\theta$ for the circularly polarized light. $\vec{k}_{\mathrm{TPP}}$ is the wavevector of the TPP wave, and κ is the damping factor along z axis.

The total electric field at the center of the spiral nanoantenna array is the superposition of the radiation from each single nanoantenna pair. When the number of nanoantenna pairs is large enough, the sum can be substituted by an integral. Under the circularly polarized light illumination, the polarization angle $\varphi = 0$, and the electric field at the center can be approximately calculated as

$$\begin{aligned} \vec{E}(\rho, \alpha, z) &= E_0 e^{-\kappa z + k_{\mathrm{TPP}} r_0} \int e^{i[(1\pm1)\theta - k_{\mathrm{TPP}} \rho \cos(\alpha - \theta)]} d\theta \\ &= 6\pi E_0 e^{-\kappa z + k_{\mathrm{TPP}} r_0} e^{i(1\pm1)\alpha} J_{1\pm1}(k_{\mathrm{TPP}} \rho) \end{aligned} \tag{17}$$

Optics EXPRESS

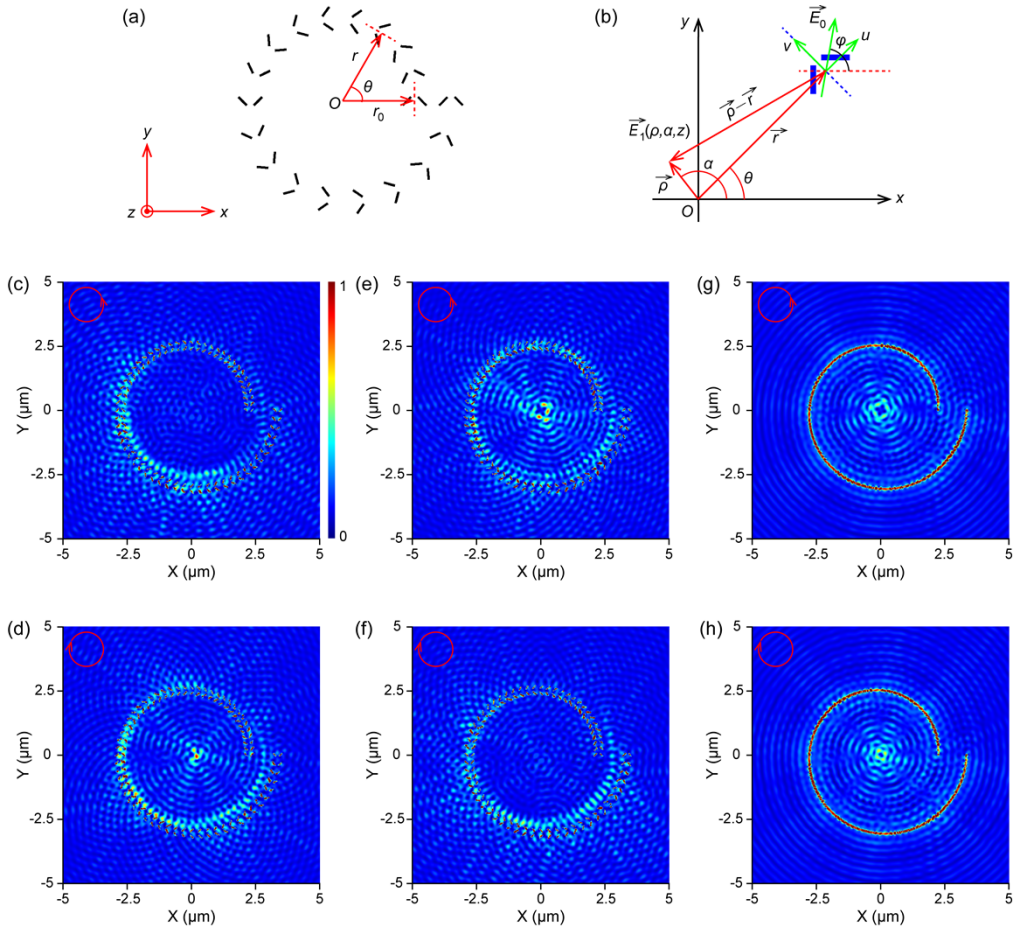

Fig. 7. Spiral nanoantenna array. (a) Schematic of the spiral nanoantenna array; (b) Schematic of the radiation from a single nanoantenna pair; (c,d) Electric field intensity distribution launched by the type-1 spiral nanoantenna array under LCP (c) and RCP (d) excitation; (e,f) Electric field intensity distribution launched by the type-2 spiral nanoantenna array under LCP (e) and RCP (f) excitation; (g,h) Electric field intensity distribution launched by the single spiral groove under LCP (g) and RCP (h) excitation. (c–h) share the same normalized color scale bar.

where $J_{1\pm1}$ is the zero-order (1–1) or the second-order (1 + 1) Bessel function. J_2 and J_0 correspond to the LCP and RCP excitation, respectively. Equation (17) indicates that the electric field distribution is strongly dependent on the polarization of the incident light. The electric field intensity launched by two types of spiral nanoantenna array is shown in Fig. 7(c–f). For type-1 spiral nanoantenna array, the initial nanoantenna pair ($\theta = 0$) consists of two nanoslits with orientations of 135° and 45° (Fig. 7(c,d)). For type-2 spiral nanoantenna array, the initial nanoantenna pair consists of two nanoslits with orientations of 45° and 135° (Fig. 7(e,f)). The electric field intensity approaches zero within the spiral for type-1 nanoantenna array under LCP excitation (Fig. 7(c)) and for type-2 nanoantenna array under RCP excitation (Fig. 7(f)). There is a bright focal point at the center of the spiral for type-1 nanoantenna array under RCP excitation (Fig. 7(d)), which corresponds to the J_0 focus. There is a bright irregular circle around the center for type-2 nanoantenna array under LCP excitation (Fig. 7(e)), which corresponds to the

Optics EXPRESS

J_2. These simulation results match well with our theoretical analysis. In contrast, a single spiral groove exhibits tighter focus under RCP excitation (Fig. 7(h)) than that under LCP excitation (Fig. 7(g)). However, the electric field enhancement around the center is relatively low in the case of single spiral groove. In comparison with the single spiral groove, spiral nanoantenna array is able to discriminate the polarization states of incident light more clearly and achieve directional focusing of TPP wave more efficiently.

4. Conclusion

In summary, the generation and propagation properties of TPPs are numerically investigated in this study. TPPs are successfully excited on a structure which consists of a silver film, DBR multilayers and a dielectric substrate. The propagation property of TPPs is explored by introducing different nanoantennas within the Ag film. With the aid of nanoantenna pairs consisting of two nanoslits, TPP wave can propagate directionally under incident light with different circular polarizations. By combining nanoantenna array with FZP, asymmetric focusing and asymmetric double focusing of TPP wave is observed. In addition, radial unidirectional coupling of TPP wave can be achieved when the nanoantenna couplers are arranged along a circular shape or a spiral shape, which can discriminate the incident polarization states clearly and present superior focusing ability compared to a single circular or spiral groove since the electric field intensity at the focal point is 4 times larger. In comparison with SPPs, TPPs exhibit superior propagation property such as higher excitation efficiency and lower propagation loss. Taken together, TPPs can be a promising supplement to SPPs in near-field manipulation of light. The numerical investigation of TPPs shows that TPPs present considerable potential in applications for polarization state analysis, chiral structure detection, integrated photonics, and on-chip device design.

Funding. National Natural Science Foundation of China (61805165, 61905147, 61935013, 61975128, 62275167, 92250304, U1701661); Natural Science Foundation of Guangdong Province (2019TQ05X750, 2020A1515010598); Science, Technology and Innovation Commission of Shenzhen Municipality (20200803150227003); China Postdoctoral Science Foundation (2022M710097).

Acknowledgments. The authors would like to acknowledge the Photonics Center of Shenzhen University for technical support.

Disclosures. The authors declare no conflicts of interest.

Data availability. Data underlying the results presented in this paper are not publicly available at this time but may be obtained from the authors upon reasonable request.

References

1. Y. Meng, Y. Z. Chen, L. H. Lu, Y. M. Ding, A. Cusano, J. A. Fan, Q. M. Hu, K. Y. Wang, Z. W. Xie, Z. T. Liu, Y. M. Yang, Q. Liu, M. L. Gong, Q. R. Xiao, S. L. Sun, M. M. Zhang, X. C. Yuan, and X. J. Ni, "Optical meta-waveguides for integrated photonics and beyond," Light: Sci. Appl. **10**(1), 235 (2021).
2. E. Bermúdez-Ureña, G. Tutuncuoglu, J. Cuerda, C. L. C. Smith, J. Bravo-Abad, S. I. Bozhevolnyi, A. F. i Morral, F. J. García-Vidal, and R. Quidant, "Plasmonic waveguide-integrated nanowire laser," Nano Lett. **17**(2), 747–754 (2017).
3. J. Langer, D. J. de Aberasturi, and J. Aizpurua, *et al.*, Present and future of surface-enhanced Raman scattering," ACS Nano **14**(1), 28–117 (2020).
4. S.-Y. Ding, E.-M. You, Z.-Q. Tian, and M. Moskovits, "Electromagnetic theories of surface-enhanced Raman spectroscopy," Chem. Soc. Rev. **46**(13), 4042–4076 (2017).
5. J.-F. Li, C.-Y. Li, and R. F. Aroca, "Plasmon-enhanced fluorescence spectroscopy," Chem. Soc. Rev. **46**(13), 3962–3979 (2017).
6. J. Dong, Z. L. Zhang, H. R. Zheng, and M. T. Sun, "Recent progress on plasmon-enhanced fluorescence," Nanophotonics **4**(4), 472–490 (2015).
7. G. X. Li, S. Zhang, and T. Zentgraf, "Nonlinear photonic metasurfaces," Nat. Rev. Mater. **2**(5), 17010 (2017).
8. M. Kauranen and A. V. Zayats, "Nonlinear plasmonics," Nat. Photonics **6**(11), 737–748 (2012).
9. M. I. Stockman, "Nanoplasmonic sensing and detection," Science **348**(6232), 287–288 (2015).
10. Y. Huang, S. C. Zhong, T. T. Shi, Y.-C. Shen, and D. X. Cui, "HR-Si prism coupled tightly confined spoof surface plasmon polaritons mode for terahertz sensing," Opt. Express **27**(23), 34067–34078 (2019).
11. K. A. Willets, A. J. Wilson, V. Sundaresan, and P. B. Joshi, "Super-resolution imaging and plasmonics," Chem. Rev. **117**(11), 7538–7582 (2017).

Optics EXPRESS

12. X. Q. Sun, H. Y. Liu, L. W. Jiang, R. X. Wei, X. Wang, C. Wang, X. C. Lu, and C. J. Huang, "Detecting a single nanoparticle by imaging the localized enhancement and interference of surface plasmon polaritons," Opt. Lett. **44**(23), 5707–5710 (2019).
13. W. Choi, Y. Jo, J. Ahn, E. Seo, Q.-H. Park, Y. M. Jhon, and W. Choi, "Control of randomly scattered surface plasmon polaritons for multiple-input and multiple-output plasmonic switching devices," Nat. Commun. **8**(1), 14636 (2017).
14. B. W. Dong, Y. M. Ma, Z. H. Ren, and C. K. Lee, "Recent progress in nanoplasmonics-based integrated optical micro/nano-systems," J. Phys. D: Appl. Phys. **53**(21), 213001 (2020).
15. Y. Q. Zhang, C. J. Min, X. J. Dou, X. Y. Wang, H. P. Urbach, M. G. Somekh, X. C. Yuan, and S.-Y. Ding, "Plasmonic tweezers: for nanoscale optical trapping and beyond," Light: Sci. Appl. **10**(1), 59 (2021).
16. Y. T. Ren, Q. Chen, M. J. He, X. Z. Zhang, H. Qi, and Y. Y. Yan, "Plasmonic optical tweezers for particle manipulation: principles, methods, and applications," ACS Nano **15**(4), 6105–6128 (2021).
17. O. Gazzano, S. Michaelis de Vasconcellos, K. Gauthron, C. Symonds, J. Bloch, P. Voisin, J. Bellessa, A. Lemaître, and P. Senellart, "Evidence for confined Tamm plasmon modes under metallic microdisks and application to the control of spontaneous optical emission," Phys. Rev. Lett. **107**(24), 247402 (2011).
18. M. Kaliteevski, I. Iorsh, S. Brand, R. A. Abram, J. M. Chamberlain, A. V. Kavokin, and I. A. Shelykh, "Tamm plasmon-polaritons: Possible electromagnetic states at the interface of a metal and a dielectric Bragg mirror," Phys. Rev. B **76**(16), 165415 (2007).
19. M. E. Sasin, R. P. Seisyan, M. A. Kalitteevski, S. Brand, R. A. Abram, J. M. Chamberlain, A. Y. Egorov, A. P. Vasil'ev, V. S. Mikhrin, and A. V. Kavokin, "Tamm plasmon polaritons: slow and spatially compact light," Appl. Phys. Lett. **92**(25), 251112 (2008).
20. M. Kaliteevski, S. Brand, R. A. Abram, I. Iorsh, A. V. Kavokin, and I. A. Shelykh, "Hybrid states of Tamm plasmons and exciton polaritons," Appl. Phys. Lett. **95**(25), 251108 (2009).
21. C. Symonds, G. Lheureux, J. P. Hugonin, J. J. Greffet, J. Laverdant, G. Brucoli, A. Lemaitre, P. Senellart, and J. Bellessa, "Confined Tamm plasmon lasers," Nano Lett. **13**(7), 3179–3184 (2013).
22. K. J. Lee, J. W. Wu, and K. Kim, "Enhanced nonlinear optical effects due to the excitation of optical Tamm plasmon polaritons in one-dimensional photonic crystal structures," Opt. Express **21**(23), 28817–28823 (2013).
23. C.-H. Xue, H.-T. Jiang, H. Lu, G.-Q. Du, and H. Chen, "Efficient third-harmonic generation based on Tamm plasmon polaritons," Opt. Lett. **38**(6), 959–961 (2013).
24. B. I. Afinogenov, V. O. Bessonov, and A. A. Fedyanin, "Second-harmonic generation enhancement in the presence of Tamm plasmon-polaritons," Opt. Lett. **39**(24), 6895–6898 (2014).
25. G. Lheureux, S. Azzini, C. Symonds, P. Senellart, A. Lemaître, C. Sauvan, J.-P. Hugonin, J.-J. Greffet, and J. Bellessa, "Polarization-controlled confined Tamm plasmon lasers," ACS Photonics **2**(7), 842–848 (2015).
26. H. Lu, X. T. Gan, B. H. Jia, D. Mao, and J. L. Zhao, "Tunable high-efficiency light absorption of monolayer graphene via Tamm plasmon polaritons," Opt. Lett. **41**(20), 4743–4746 (2016).
27. C.-H. Xue, F. Wu, H.-T. Jiang, Y. H. Li, Y.-W. Zhang, and H. Chen, "Wide-angle spectrally selective perfect absorber by utilizing dispersionless Tamm plasmon polaritons," Sci. Rep. **6**(1), 39418 (2016).
28. H. Lu, X. T. Gan, D. Mao, Y. C. Fan, D. X. Yang, and J. L. Zhao, "Nearly perfect absorption of light in monolayer molybdenum disulfide supported by multilayer structures," Opt. Express **25**(18), 21630–21636 (2017).
29. H. Lu, Y. W. Li, Z. J. Yue, D. Mao, and J. L. Zhao, "Topological insulator based Tamm plasmon polaritons," APL Photonics **4**(4), 040801 (2019).
30. M. Z. He, J. R. Nolen, J. Nordlander, A. Cleri, N. S. Mcllwaine, Y. C. Tang, G. Y. Lu, T. G. Folland, B. A. Landman, J.-P. Maria, and J. D. Caldwell, "Deterministic inverse design of Tamm plasmon thermal emitters with multi-resonant control," Nat. Mater. **20**(12), 1663–1669 (2021).
31. Z.-Y. Yang, S. Ishii, T. Yokoyama, T. D. Dao, M.-G. Sun, P. S. Pankin, I. V. Timofeev, T. Nagao, and K.-P. Chen, "Narrowband wavelength selective thermal emitters by confined Tamm plasmon polaritons," ACS Photonics **4**(9), 2212–2219 (2017).
32. Z. Y. Wang, J. K. Clark, Y.-L. Ho, B. Vilquin, H. Daiguji, and J.-J. Delaunay, "Narrowband thermal emission realized through the coupling of cavity and Tamm plasmon resonances," ACS Photonics **5**(6), 2446–2452 (2018).
33. X. Zhang, X.-S. Zhu, and Y.-W. Shi, "An optical fiber refractive index sensor based on the hybrid mode of Tamm and surface plasmon polaritons," Sensors **18**(7), 2129 (2018).
34. M. M. Keshavarz and A. Alighanbari, "Terahertz refractive index sensor based on Tamm plasmon-polaritons with graphene," Appl. Opt. **58**(13), 3604–3612 (2019).
35. M. M. Keshavarz and A. Alighanbari, "Self-referenced terahertz refractive index sensor based on a cavity resonance and Tamm plasmonic modes," Appl. Opt. **59**(14), 4517–4526 (2020).
36. Q. Q. Liu, X. C. Zhao, C. L. Li, X. L. Zhou, Y. Chen, S. W. Wang, and W. Lu, "Coupled Tamm plasmon polaritons induced narrow bandpass filter with ultra-wide stopband," Nano Res. **15**(5), 4563–4568 (2022).
37. Z. A. Zaky, A. Sharma, and A. H. Aly, "Tamm plasmon polariton as refractive index sensor excited by gyroid metals/porous Ta2O5 photonic crystal," Plasmonics **17**(2), 681–691 (2022).
38. Z. A. Zaky, M. R. Singh, and A. H. Aly, "Tamm resonance excited by different metals/graphene," Photonics Nanostructures: Fundam. Appl. **49**, 100995 (2022).
39. C.-Z. Deng, Y.-L. Ho, Y.-C. Lee, Z. Y. Wang, Y.-H. Tai, M. Zyskowski, H. Daiguji, and J.-J. Delaunay, "Two-pair multilayer Bloch surface wave platform in the near- and mid-infrared regions," Appl. Phys. Lett. **115**(9), 091102 (2019).

Optics EXPRESS

40. R. X. Wang, Y. Wang, D. G. Zhang, G. Y. Si, L. F. Zhu, L. P. Du, S. S. Kou, R. Badugu, M. Rosenfeld, J. Lin, P. Wang, H. Ming, X. C. Yuan, and J. R. Lakowicz, "Diffraction-free Bloch surface waves," ACS Nano **11**(6), 5383–5390 (2017).
41. F. Feng, G. Y. Si, C. J. Min, X. C. Yuan, and M. Somekh, "On-chip plasmonic spin-Hall nanograting for simultaneously detecting phase and polarization singularities," Light: Sci. Appl. **9**(1), 95 (2020).
42. B. Zhao and Z. M. Zhang, "Strong plasmonic coupling between graphene ribbon array and metal gratings," ACS Photonics **2**(11), 1611–1618 (2015).
43. J. G. Hu, E. X. Yao, W. Q. Xie, W. Liu, D. M. Li, Y. H. Lu, and Q. W. Zhan, "Strong longitudinal coupling of Tamm plasmon polaritons in graphene/DBR/Ag hybrid structure," Opt. Express **27**(13), 18642–18652 (2019).
44. J. Lin, J. P. B. Mueller, Q. Wang, G. H. Yuan, N. Antoniou, X.-C. Yuan, and F. Capasso, "Polarization-controlled tunable directional coupling of surface plasmon polaritons," Science **340**(6130), 331–334 (2013).
45. F. Feng, S.-B. Wei, L. Li, C.-J. Min, X.-C. Yuan, and M. Somekh, "Spin-orbit coupling controlled near-field propagation and focusing of Bloch surface wave," Opt. Express **27**(20), 27536–27545 (2019).
46. Q. B. Jiang, A. Pham, M. Berthel, S. Huant, J. Bellessa, C. Genet, and A. Drezet, "Directional and singular surface plasmon generation in chiral and achiral nanostructures demonstrated by leakage radiation microscopy," ACS Photonics **3**(6), 1116–1124 (2016).
47. B. Wild, L. Cao, Y. G. Sun, B. P. Khanal, E. R. Zubarev, S. K. Gray, N. F. Scherer, and M. Pelton, "Propagation lengths and group velocities of plasmons in chemically synthesized gold and silver nanowires," ACS Nano **6**(1), 472–482 (2012).
48. S.-Y. Lee, K. Kim, S.-J. Kim, H. Park, K.-Y. Kim, and B. Lee, "Plasmonic meta-slit: shaping and controlling near-field focus," Optica **2**(1), 6–13 (2015).
49. W. B. Chen, R. L. Nelson, and Q. W. Zhan, "Efficient miniature circular polarization analyzer design using hybrid spiral plasmonic lens," Opt. Lett. **37**(9), 1442–1444 (2012).
50. J. R. Zhang, Z. Y. Guo, R. Z. Li, W. Wang, A. J. Zhang, J. L. Liu, S. L. Qu, and J. Gao, "Circular polarization analyzer based on the combined coaxial Archimedes' spiral structure," Plasmonics **10**(6), 1255–1261 (2015).
51. J. R. Zhang, Z. Y. Guo, K. Y. Zhou, L. L. Ran, L. Zhu, W. Wang, Y. X. Sun, F. Shen, J. Gao, and S. T. Liu, "Circular polarization analyzer based on an Archimedean nano-pinholes array," Opt. Express **23**(23), 30523–30531 (2015).
52. Q. Zhang, P. Y. Li, Y. Y. Li, X. R. Ren, and S. Y. Teng, "A universal plasmonic polarization state analyzer," Plasmonics **13**(4), 1129–1134 (2018).